DARPA SWEEPER Final Technical Report

Award Number: HR0011-10-2-0002

PI:
Prof. Ming C. Wu
University of California, Berkeley

Period:
September 2010 to December 2014

Table of Contents

1. Introduction

The goal of this project is to develop MEMS-based high-speed (MHz) optical phased arrays (OPAs). The OPAs have emerged as a powerful technology for agile, high-resolution, random-access pointing/tracking with multiple simultaneous beams. Applications of OPAs range from 3D display and printing, optical data-storage, telecommunication to military and other industrial applications. A wide variety of technologies have been developed for OPAs. The most mature OPAs are based on liquid crystals. They are low cost, and can be readily integrated on electronic integrated circuit drivers. The so-called liquid crystal on silicon (LCoS) technology has been used for both microdisplays as well as OPAs. However, the liquid crystal-based OPAs have some drawbacks, including slow response time, fringe field effect, and low steering efficiency at large angles. Recently, compact OPAs using silicon photonic waveguides on a silicon-on-insulator (SOI) with either wavelength tuning or thermo-optic phase modulation. Large arrays have been made using silicon integrated circuit foundries. For wavelength-tuning approach, the beam direction is dependent on wavelength, and it is not possible to achieve monochromatic beamsteering. Phase tuning using thermo-optic modulators overcome this limit, however, it suffers from high power consumption, particularly for large arrays. In addition, the maximum optical powers in silicon photonic OPAs are limited by the power handling capability of sub-micron-sized waveguides.

The key idea in this program is to leverage on the lightweight high-contrast grating (HCG) mirrors to enable high-speed actuation. The HCG mirror consists of a single layer of sub-wavelength gratings made of high-refractive index materials, such as GaAs or Si, with a thickness typically much smaller than a micron. The HCG mirrors have higher reflectivity than conventional distributed Bragg reflectors (DBRs) and broader reflection band. Their masses are 100x lighter than the DBR's. Since the mechanical resonance frequency is proportional to the square root of the ratio of spring constant and mirror mass, much faster operation is expected for HCG mirrors. Our OPA is based on free-space optics, and is compatible with a wide variety of laser sources and imaging modalities.

In this program, we have successfully developed three generations of MEMS HCG SWEEPER OPAs, and have developed a unique interferometric imaging system to measure the phase shift of individual pixels in the array. It also allows close-loop control of the phases of all mirror pixels in the OPA. We will describe the key results we have achieved in each of these areas.

2. Si-based 8x8 OPA with Single HCG Mirror Phase Shifters

The principle of MEMS phased arrays for beamsteering is schematically depicted in Figure 1. Light is normally incident on the 8×8 array of HCG mirrors that are electrostatically actuated toward the substrate. The light is reflected back and its phase (φ) is modulated to alter the shape of the reflected light wavefront. This phase modulation enables not only to steer the propagation direction of the light, but also to focus.
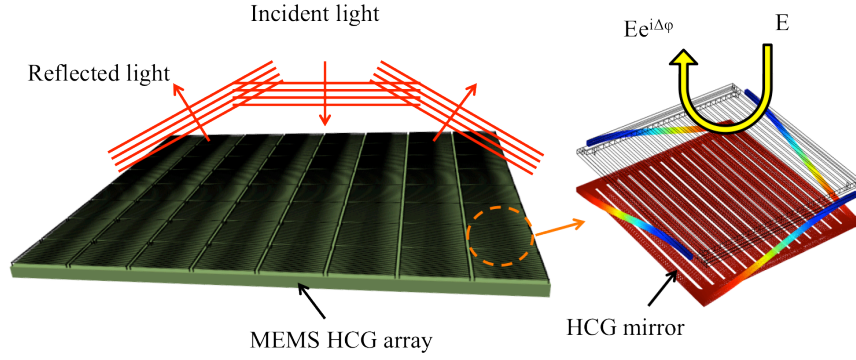
Figure 1. Schematic view of MEMS phased array composed of high contrast grating mirrors.

In particular, HCGs have become a subject of special interest regarding their very high reflectivity along a broad bandwidth, wider than DBR, as illustrated in Figure 2. The HCG and DBR are both designed to reach 99.9% reflectivity at 1550 nm. The dimensions of HCG are chosen so that it has 99.9% reflectivity for transverse-electric (TE)-polarized light of 1550 nm wavelength via extensive investigations on the duty cycle and thickness of gratings using the rigorous coupled wave analysis (RCWA) method. The physical mechanism behind the high reflectivity of HCG is shown in the inset of Figure 2. The incident light excites multiple (typically two) optical modes within the HCG. As these modes reach the bottom of the HCG, they interfere destructively, which prevents the transmitted wave from being launched, thus resulting in ~100% of the power to be reflected. A reflectivity higher than 99% can be maintained over a broad wavelength range of $\Delta\lambda/\lambda \sim 30\%$ as reported in [6]. For comparison: a reflectivity as high as 99% for a DBR typically requires 20 to 40 pairs of alternating index materials, resulting in ~100 times heavier reflector than an HCG. Because of its low mass, the HCG has advantages as a very fast MEMS mirror.
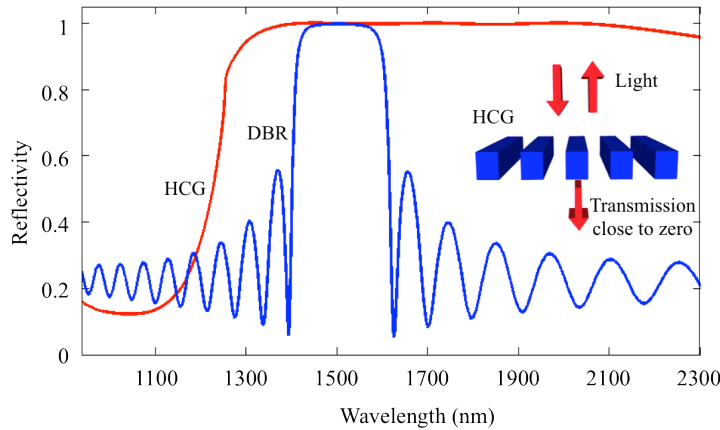

Figure 2. Reflectance spectrum of an HCG compared to a DBR. The inset illustrates the simplified principle of reflection.

The specific design of the HCG for our MEMS phased array is as follows: period = 1380 nm, width = 670 nm and thickness = 320 nm. The mirror, 20×20 µm², is tethered to four anchors with four springs. The width and thickness of the springs are designed to be 350 nm and 320 nm, respectively. The lengths of the two beam

segments in each spring are 18.35 μm and 350 nm. With the fixed spring constant based on the dimensions above, k = 1.188 N/m, the lightweight grating structure can be designed to attain a resonant frequency of 451 kHz thanks to its low mass, 139 pg.

Our optical phased arrays are fabricated using a SOI wafer with 320 nm-thick device layer and 2 μm-thick buried oxide (BOX) layer. Only one photolithography mask is used in the fabrication process, resulting in easy fabrication, high yield and low cost. After a standard cleaning process with sulfuric peroxide mixture and buffered hydrofluoric (HF) acid, the device layer of a SOI wafer is heavily doped using solid boron in a furnace to be 23 Ω/sq, providing electrical lines of low electrical resistance. Using a deep ultraviolet (DUV) ASML300 stepper, the top silicon layer of the SOI wafer is patterned with the phased array. Then, anisotropic dry etching follows and HF vapor etching is used to remove the BOX layer, releasing the HCGs. The HF vapor etching process requires anchors that are large enough to have some BOX layer remain underneath while the 2 μm-thick BOX layer under the HCGs is totally removed and the HCGs are released. However, large anchors will reduce the maximum beamsteering angle imposed by the mirror pitch. Therefore, two separate anisotropic dry etching steps are applied, one for the device layer and another for the partial BOX layer. First, dry etching of silicon is performed to define 320 nm-deep OPA patterns on the device layer using Cl_2 and HBr. Second, an anisotropic dry etching using CF_4 follows to partially etch the BOX layer in the vertical direction to shorten the release process time of isotropic etching using HF vapor. With only the isotropic HF vapor etching, very large anchors would be required to be able to survive until the silicon ground plane is revealed, resulting in low fill-factor.
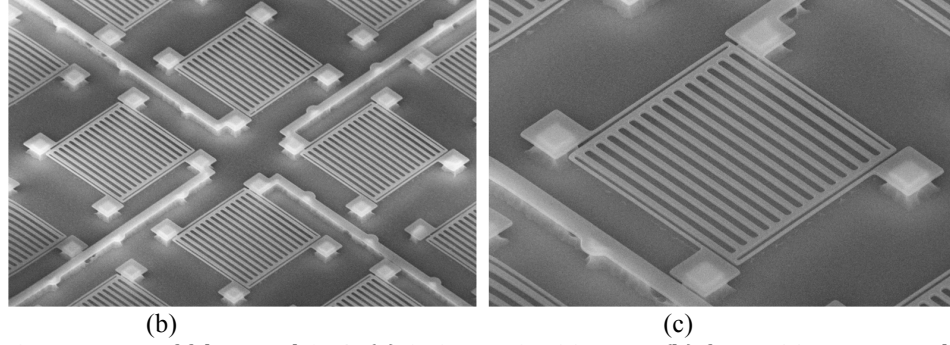

(a)

(b)   (c)
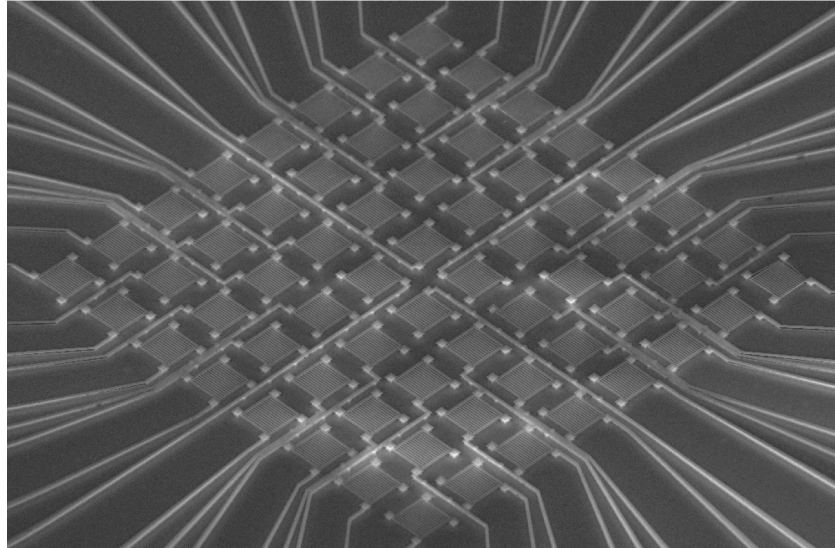
Figure 3. SEM images of fabricated OPA. (a) 8×8 MEMS HCG array, (b) four HCG mirrors and electrical lines connected via the anchors, (c) HCG mirror with four mechanical springs showing remaining BOX layer beneath each of the four anchors.

Figure 3(a) shows the fabrication result of a phased array composed of 64 HCG mirrors. The electrical addressing lines are designed to be wide enough not to be released during HF vapor etching. Anchors are sufficiently large for the same reason. The pitch of the OPA is designed to be 35 μm. Figure 3(b) and (c) show enlarged views of individual mirrors, showing the delicate thin grating bars of the HCGs. The oxide undercuts can be seen through the thin silicon device layer. When the oxide undercut is too great, the 2 μm wide electrical lines are not supported by the BOX layer. When applying voltage to these over-etched samples, some electrical lines snap into contact with the grounded substrate, leading to a short circuit. Therefore, sufficient anisotropic dry etching of oxide is required prior to HF vapor release. However, the dry etch has relatively low selectivity between oxide and silicon, resulting in thinned and narrowed silicon springs due to the large openings around the HCG. As a result, the spring constant becomes lower than designed. We measured resonant frequencies using a commercial laser Doppler vibrometer (LDV) system. The average resonant frequency of the phased array is measured to be 317.15 kHz. Its standard deviation is 5.93 kHz, equivalent to 1.8 %.

We measured the HCG time response, shown in Figure 4, with the interferometer. A 20-μs-long voltage pulse is applied to the HCG, resulting in a displacement of the mirror and a shift in optical phase. The mirror exhibits ringing after each transition. The motion is fitted to a damped harmonic oscillator model. The frequency and damping of the ringing is different after switching on or off. This difference is caused by the change in resonant frequency of the electrostatically-actuated MEMS HCG when the voltage varies, because its effective spring constant depends on the applied voltage. Based on the fitted curve, the frequency of oscillation after transition from the on state to the off state is 314 kHz ($1/f$ = 3.18 μs), which is in good agreement with the measured resonant frequency of the MEMS HCG, 317.15 kHz, in Fig. 5. The frequency of the ringing after transition from the off state to the on state is 171 kHz ($1/f$ = 5.83 μs), implying that effective spring constant decreases when the voltage is on. The motion is almost critically damped, even at this high frequency, without vacuum packaging.
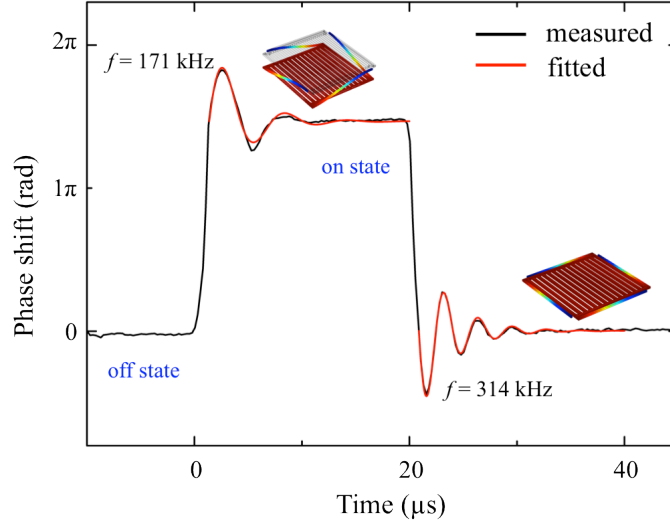
Figure 4. Comparison of measured time response and damped harmonic oscillator fitting

For a normally incident beam, the beamsteering angle is expected to be $\sin\theta = \pm\frac{\lambda}{2\Lambda}$, where λ is the design wavelength for the phased array, 1550 nm, and Λ is the mirror pitch, 35 μm. The maximum steering angle is expected to be ±1.32°. The total field of view is magnified to ±10° via a pair of achromatic doublet lenses. Figure 5(a) shows a quadrant of the optical output from the phased array when no voltage is applied. The unbiased phased array provides a strong zeroth order beam and grating sidelobes at 20° in both x and y directions in Figure 5(a). Figure 5(b) depicts a quadrant of the optical output of the maximum beamsteering angle, 10°, along the horizontal axis. As is shown in the inset of Figure 5(b), 18 V is applied to every other column to achieve 0 and π phase shift in alternating columns in the phase map. Figure 5(c) presents the maximum beamsteering angle along the vertical axis using the phase map in the inset. Cross-sectional views of the camera images are converted to the graphs in Fig. 8 (d) and (e), showing that the beam width is 2°. The measured beamsteering angles and widths match very well with the theoretical predictions.
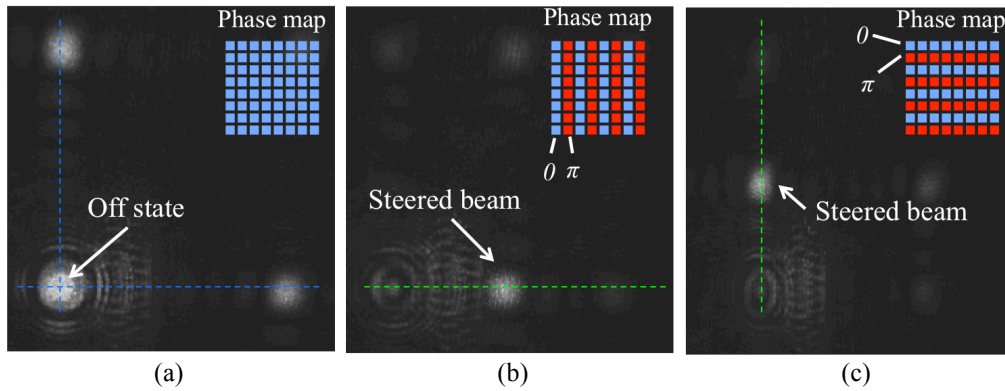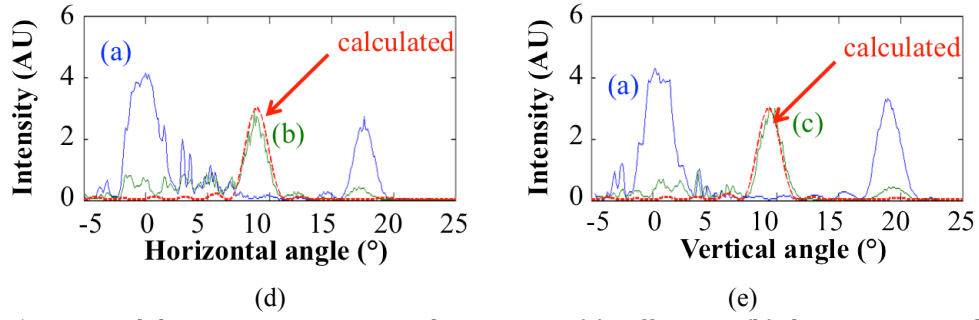
Figure 5.Measured beamsteering in two dimensions. (a) off state, (b) beamsteering along the horizontal axis, (c) beamsteering along the vertical axis, (d, e) comparison of measured and calculated intensity along the horizontal (resp. vertical) axis.

To summarize, the 8×8 phased array with MEMS HCG mirrors has been fabricated on a SOI wafer, characterized its resonant frequency and time response, and demonstrated 10° beamsteering in two dimensions. The HCG is designed to have 99.9 % reflectivity at a wavelength of 1550 nm and maintains such high reflection along a wider bandwidth than a DBR. Thanks to the low mass of HCGs on a SOI wafer, a fast time response is attained, on the order of microseconds. The single layer HCGs are resistant to thermally induced stress.

3.   Si-Based 32x32 OPA with Single HCG Mirror Phase Shifters

In this section, we describe a 32x32 MEMS OPA with high fill-factors and microsecond response time. To reduce the mirror weight and temperature-dependent curvature, we use HCG mirrors comprising a single layer of sub-wavelength polysilicon gratings with 400 nm thickness, 1250 nm pitch, and 570 nm grating bar width. The mirror has a broad reflection band and a peak reflectivity of 99.9% at 1550 nm wavelength. With 20×20 µm2 pixels and 2 µm, the OPA has a total aperture of 702×702 µm^2 and a fill factor of 85%. The OPA is electrostatically controlled by voltage and has a total field of view of ±2°, an instantaneous field of view (beam width) of 0.14°, and a response time of 3.8 µs. The latter agrees well with the mechanical resonance frequency of the HCG mirror (0.42 MHz).

The MEMS OPA comprises a 32×32 array of HCG mirrors. Figure 6(a) shows the top view of the OPA layout. Each HCG mirror is tethered to four mechanical springs, one at each corner. The mirrors are electrostatically actuated by applying a voltage between the mirror and the substrate. The mirrors in the same column are electrically connected via their springs and move together when a voltage is applied. As a result, the current OPA can perform one-dimensional beamforming. Potentially, an individually addressable electrode array can be integrated underneath the HCG mirrors for two-dimensional beamforming. Figure 6(b) shows an optical image of the released array. Here, every other row of the OPA has been pulled downwards by electrostatic actuation, creating a periodic phase shift pattern.
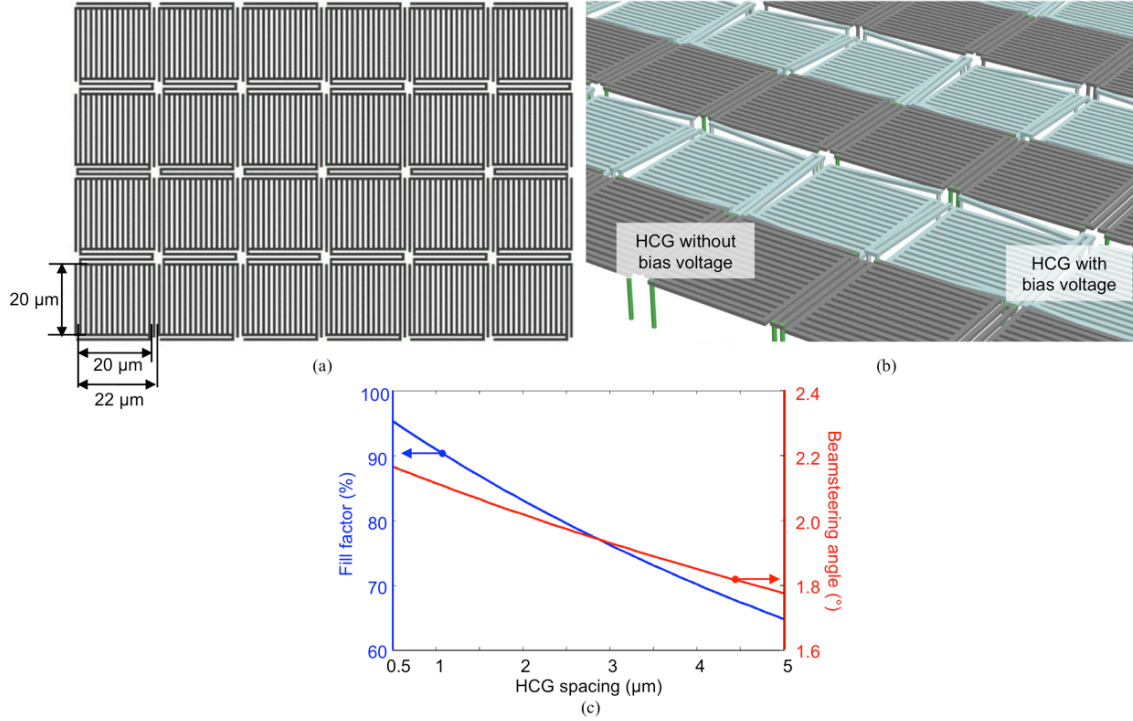
Figure 6. (a) Layout and (b) optical micrograph of 32×32 polysilicon OPA with high-contrast-grating (HCG) mirrors. (c) The fill factor and maximum steerable angle as a function of the spacing between HCG mirrors. The HCG mirror size is 20×20 μm².

For high performance OPA, it is desirable to reduce the array pitch and increase the fill-factor. The pitch determines the total field of view (TFOV), the largest angle one can steer to. High fill-factor is associated with better diffraction efficiency. Since we used the same polysilicon layer for both the HCG mirrors and the springs, the fill factor is limited by the width of the springs and the clearance between the structures. For a given spacing between HCG mirrors, the fill factor reduces with mirror size. Moreover, small MEMS mirrors require higher actuation voltage. To address these issues, the mirror area is chosen to be 20×20 μm². We use a deep ultraviolet (DUV) stepper (ASML PAS 5500/300) with a resolution of 250 nm to pattern the HCG and MEMS structures. Figure 6(c) shows the calculated fill factor and TFOV versus the mirror spacing for an OPA with 20×20 μm² mirrors. The spacing between HCG mirrors is designed to be 2 μm, resulting in a fill factor of 85% and a TFOV of ±2° at 1550 nm wavelength.
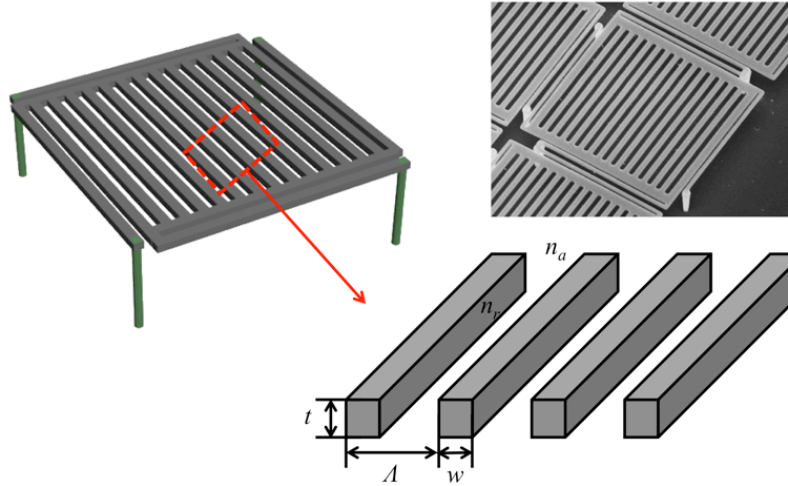
Figure 7.Schematic view and scanning electron microscope (SEM) micrograph of the HCG mirror.

The schematic and the scanning electron micrograph (SEM) of the HCG mirror are shown in Figure 7. The HCGs are of interest for a wide range of integrated optoelectronic device applications, such as lasers, filters, splitters, and couplers. In order to design the HCG used in our optical phased array, it is necessary to determine the grating period (Λ) for the desired operating wavelength (λ). For example, the diffraction regime, where the grating period (Λ) is greater or much less than the wavelength (λ) doesn't result in high reflectivity. In contrast, in the near-wavelength regime, where the period (Λ) is between λ/n_r and λ/n_a, where n_r is the refractive index of the grating bars and n_a is the refractive index of air, extraordinary features such as high reflectivity (~99.9%) and high quality-factor resonance ($Q > 10^7$) have been realized. It has been demonstrated that the reflectivity of HCGs can exceed 99% over an extraordinarily broad wavelength range of $\Delta\lambda/\lambda \sim 30\%$. For optical MEMS devices, the fact that the HCG is composed of only a single polysilicon layer eliminates the problems of residual stress and differential thermal expansion (e.g. bimorph effects) commonly observed in multi-layer reflectors.

A polysilicon surface micromachining process, shown in Figure 8, is used to fabricate our MEMS OPA. The fabrication begins with depositing a sacrificial low temperature oxide (LTO) film of 3.4 µm thickness on a silicon wafer. Then 0.3-µm-diameter holes are patterned and etched through the LTO using DUV lithography and anisotropic dry etching. 0.1-µm-thick stoichiometric silicon nitride is deposited to coat the holes in LTO for electrical isolation. The silicon nitride over the planar part of LTO is removed by chemical mechanical polishing (CMP), leaving silicon nitride only on the sidewalls of the LTO holes. The slurry used in the CMP process features very high selectivity to silicon dioxide and polysilicon so the silicon nitride filled in the holes remains while the silicon nitride on top of the LTO is removed. Polysilicon deposition is performed. The polysilicon layer is in-situ doped to a resistivity of 8×10^{-4} Ω-cm in a low-pressure chemical vapor deposition (LPCVD) furnace to achieve low electrical resistance for HCG mirrors and electrical lines. The grain sizes and therefore the surface roughness of polysilicon films deposited by

LPCVD are on the order of tens of nanometers. Thus, CMP of the polysilicon surface is required to improve feature definition (i.e. fabrication of gratings with sub-wavelength width) and reduce optical scattering loss. The polysilicon plugs filling the silicon nitride-coated holes serve as the anchors of the HCG mirrors. Repeating the DUV stepper lithography and anisotropic dry etching, the HCG array is patterned. Electrical fan-outs and wire bonding pads are also formed in the same process step. The release process is performed at the die level. The etch rate of LTO in diluted HF (49% concentrated HF:deionized water = 1:1) is measured to be ~1.1 μm/min so that 2 min dipping is sufficient to remove the LTO sacrificial layer. The device is then rinsed and dried in a critical point dryer (CPD).
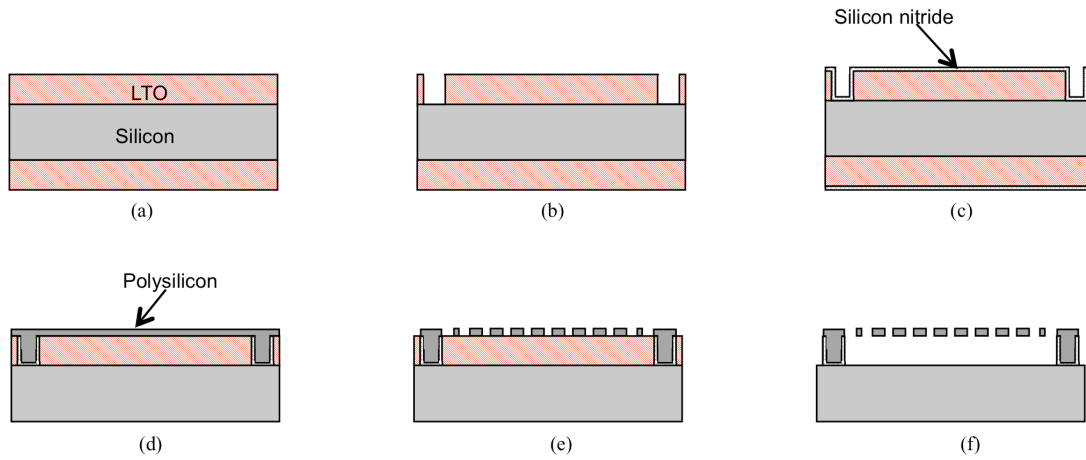
Figure 8. The fabrication process of a MEMS-actuated polysilicon optical phased array (OPA) with high-contrast-grating (HCG) mirrors
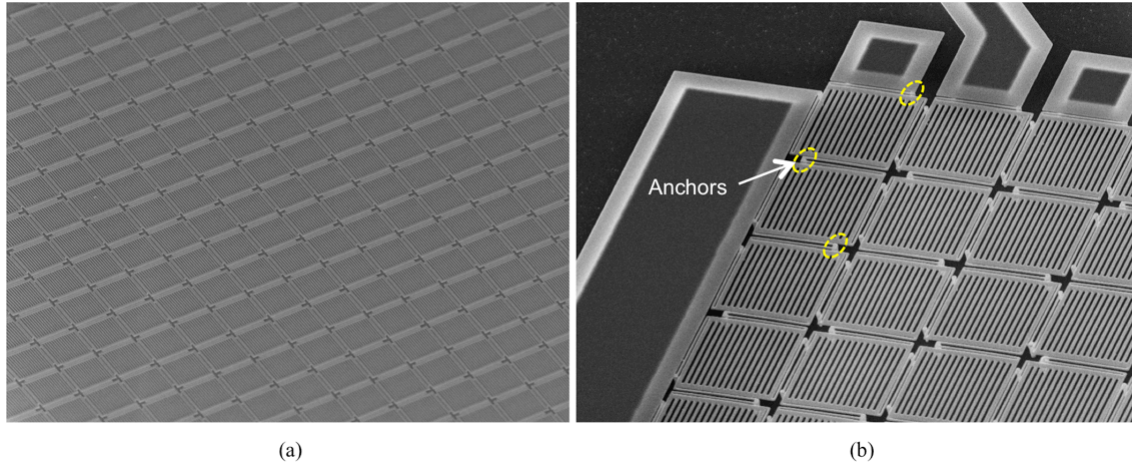
Figure 9. SEM images of the fabricated OPA: (a) 32×32 MEMS HCG array, (b) polysilicon HCG mirrors, anchors, and mechanical springs.

Figure 9(a) shows the SEM image of a released 32×32 MEMS HCG optical phased array. Figure 9(b) shows an enlarged image of the HCG mirrors. Each HCG mirror is supported by four polysilicon mechanical springs anchored by silicon nitride-coated polysilicon plugs. The mirrors are electrically insulated from the substrate, thanks

to the silicon nitride liner. To achieve high fill-factor, the HCG mirrors are electrically connected along the same row via the anchors, as marked by the yellow dotted lines in the Figure 9(b). Thirty-two gold wire-bonding pads are patterned at the edges of the die.

The experimental setup for characterizing the OPA is shown in **Error! Reference source not found.**Figure 10. It includes an imaging interferometer to measure, and subsequently control, the phase shift of each pixel. Light from a laser source is collimated and directed to the MEMS OPA. Part of the light reflected from the OPA is tapped to a measurement path where it is interfered with a reference beam to form an interferogram on a camera (Xenics Bobcat-1.7-320). The interferometer allows static and dynamic measurements of phase shift at pixel level. Figure 11(a) shows the measured temporal response of an HCG mirror in response to a 25 kHz square wave excitation at 20V. The phase response is stable to within ±10% of the final value (0.36π) within 3.8 μs following each transition. The temporal response is fitted well by a damped-harmonic oscillator model with a damping ratio of 0.2 and a damped natural frequency of 0.46 MHz.
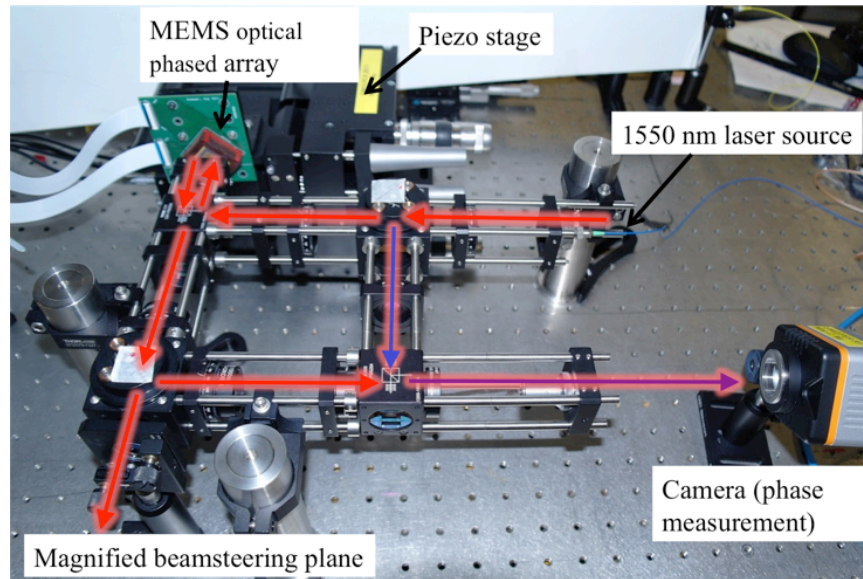

Figure 10. Optical measurement setup

Our imaging interferometer is capable of measuring the phase shifts of all mirrors within the field of view. It is a powerful tool to characterize the uniformity of the mirrors in the OPA. We have measured the temporal responses of 180 mirrors for 25 kHz square wave actuation. For each mirror, we obtained a temporal response similar to that shown in Figure 11(a). The aggregated temporal responses of all 180 mirrors are condensed in Figure 11(b). The vertical axis is the time base, and the horizontal axis is the mirror number. The phase is represented by pseudo color whose scale is shown on the right. The 180 HCG mirrors exhibit uniform phase shift and similar transient response at each phase transition, with only 2 HCG

mirrors, #29 and #45, showing different responses. The uniformity of the oscillation period is shown by the histogram in Figure 11(c). The average oscillation period is calculated to be 2.64 µs, corresponding to an average resonance frequency of 0.42 MHz. The measurement is in good agreement with the calculation based on the thickness measurement. The resonance frequency of a few representative mirrors was also measured using a LDV, as shown in Figure 11(d). The resonance frequency agrees well with the value derived from the time response. The resonance frequency of the HCG mirror is higher than conventional MEMS mirrors thanks to the lightweight HCG mirrors. The switching time can be further decreased by employing stiffer springs, allowing for even faster beamsteering.
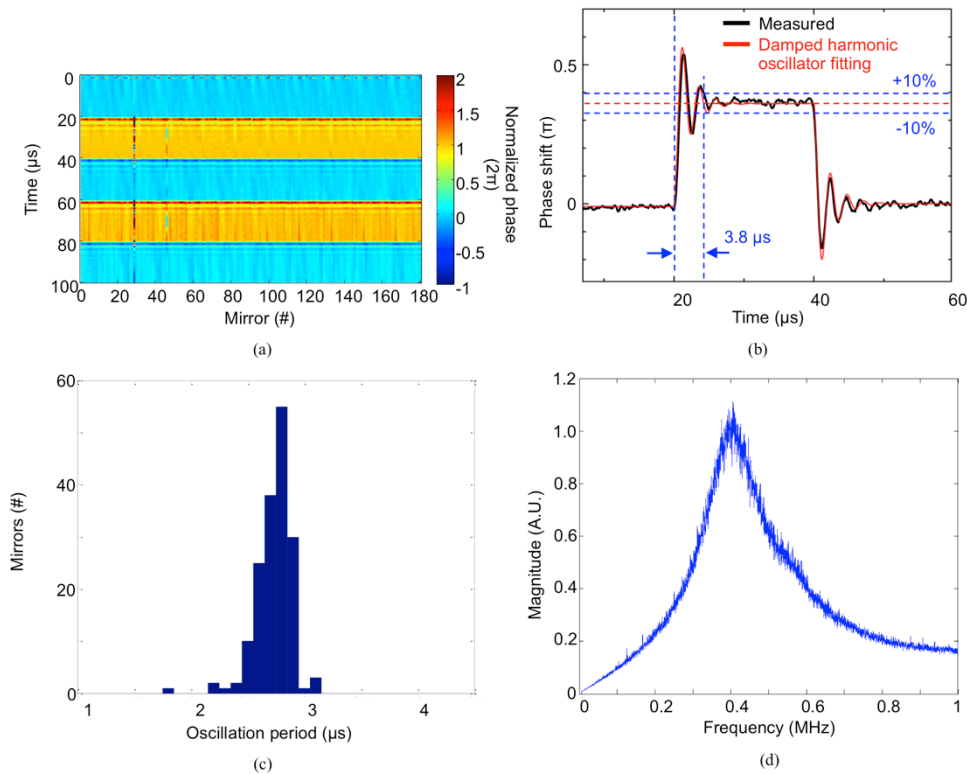

Figure 11. Static and dynamic characterization results using the MEMS OPA: (a) temporal response of an HCG mirror for a 25 kHz square wave excitation, (b) phase shifts of 180 HCG mirrors in response to 25 kHz square waves. (c) Histogram of the oscillation period. (d) Frequency response of HCG mirror measured by laser Doppler Vibrometer.

Binary phase patterns, with the phase shift of each column of mirrors set to either 0 or π, were used for one-dimensional beamsteering experiments, as shown in Figure 12(a). Figure 12(b) shows the corresponding far-field patterns. State 0 is the case when no voltage is applied to the OPA and the beam is not deflected. From State 1 to State 3, the 0th order beam is suppressed and the light is directed into symmetric diffraction orders by the binary phase pattern. The diffracted beam angle is given by $\theta = \sin^{-1}(\lambda/2N\Lambda)$ where λ = 1550 nm is wavelength of the laser, Λ = 22 µm is the mirror pitch, and $2N$ is the number of mirrors per phase period. The maximum deflection angle measured at State 3 is ±2°, which agrees well with the calculated value.

Figure 13(a) illustrates the measured intensity profile for $2N = 0$ (State 0), 2 (State 3), 4 (State 2), 8 (State 1), 12, 16, and 20. The calculated beam location matches the measured beamsteering angles in the graph. The intensity of 0th order beam (black curve) appears to be well-suppressed with beamsteering as shown in the colored curves. The diffracted intensity was studied as a function of phase shift φ applied to the mirrors at the maximum steering angle ($2N=2$). The intensity in the 1st order diffraction lobe at the maximum angle is given by $I=I_{max}\sin^2(\varphi/2)$, where the maximum intensity I_{max} occurs at $\varphi = 1\pi$. The measured intensity versus phase shift agrees very well with the theoretical calculation, as shown in Figure 13(b). Figure 13(c) shows asymmetrical beamsteering results using a linear phase ramp modulo 2π. The experiments for asymmetrical beamsteering were performed using no more than 1.2π phase shift to avoid possible unwanted pull-in during HCG actuation. Thirty-three different stair-step phase structures using the OPA implement individual beam positioning to the left and right from 0th order beam location.
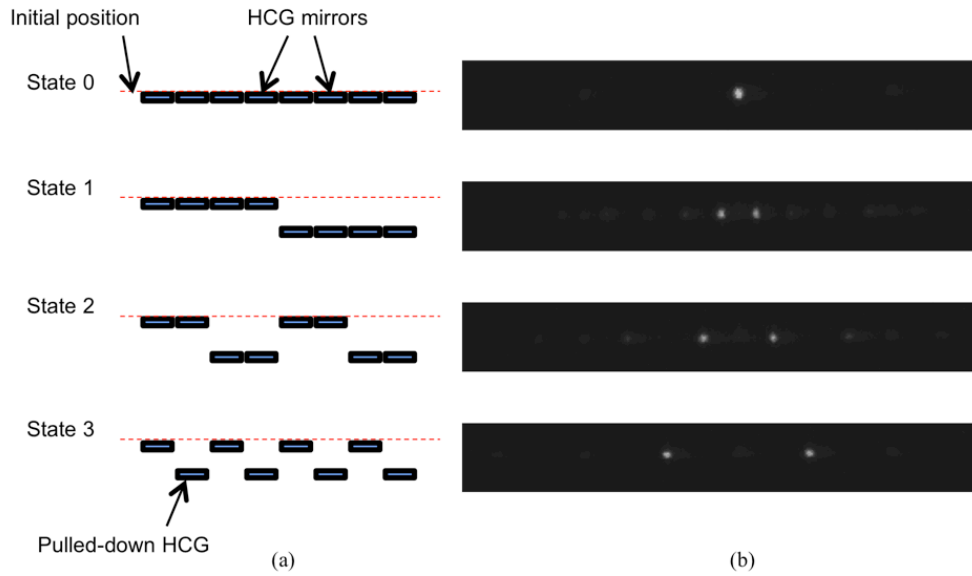

Figure 12. (a) Binary phase patterns using 0 and π phase shift for one-dimensional beamsteering, (b) Measured results of beamsteering in the far field.
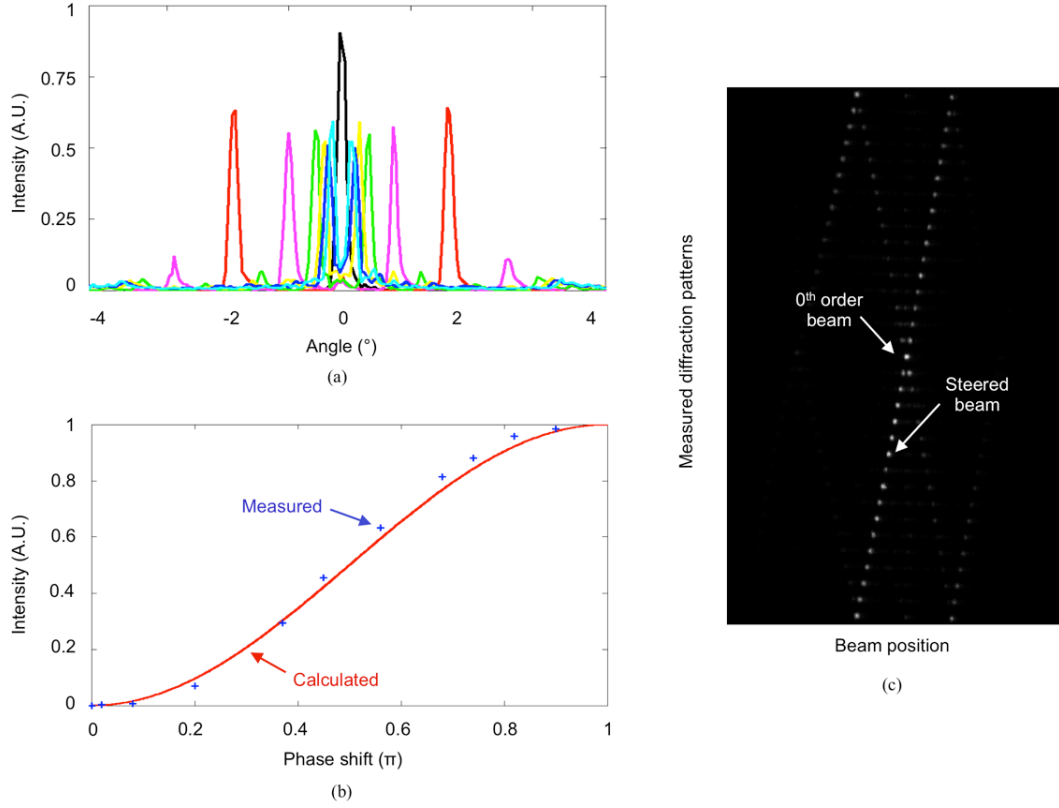
Figure 13. Beamsteering results using the 32×32 MEMS OPA: (a) intensity profile of the symmetrically steered beams, (b) measured and calculated diffraction efficiency of the steered beam at the maximum steered angle, (c) asymmetric beamsteering measurement in the far field.

4. GaAs-based OPA with All-Pass-Filter Phase Shifters

In this section, we describe the 8x8 OPA with HCG all-pass filters. The array element is an all-pass filter (APF) at 1550 nm with a HCG as a top reflector and a DBR as the bottom reflector. The incident light comes at surface normal to the APF; the phase of the reflective light can be tuned efficiently with a small actuation distance of the HCG. A phase shift as large as 1.7 π is experimentally demonstrated within 50 nm displacement of the HCG and 10 V actuation voltage, in a speed as high as 0.5 MHz. Beam steering is demonstrated by creating a near-field reflection phase pattern with different actuation voltages on individual pixels.

In previous section, the HCG has been used as a piston mirror for the OPA, where the phase of the reflection beam on the HCG can be tuned linearly with the displacement of the HCG. While this approach is simple and straightforward, a long HCG actuation distance is required for a 2π phase shift, trading off actuation voltage for high-speed operation. To overcome this disadvantage, here we construct an all-pass filter using a top HCG and bottom DBR, with carefully designed reflectivity. By replacing the uniform membrane with HCG, one gains the flexibility in controlling the mirror reflectivity and thus the cavity quality factor. By actuating the HCG to tune the length of the etalon across its Fabry-Perot (FP) resonance, the reflection

phase of the surface normal incident light experiences a continuous phase change approaching 2π, while the reflection beam power can maintain nearly the same with the incident light. The resonance effect greatly enhances the phase tuning efficiency, i.e. a small HCG displacement for a large phase shift. High speed and low actuation voltage can be achieved at the same time.

Figure 14 shows the schematic of the APF. The device is fabricated on a GaAs epitaxial wafer. The HCG is defined by electron beam lithography, and followed by a reactive ion etch on a p-doped $Al_{0.6}Ga_{0.4}As$ epitaxial layer, which is on top of an intrinsic sacrificial layer GaAs and 22 pairs of $GaAs/Al_{0.9}Ga_{0.1}As$ n-doped DBR. The sacrificial layer is subsequently selectively etched to form a FP cavity with the suspended HCG as a top mirror and DBR as a bottom mirror. To form the all-pass filter, the reflectivity of the DBR is designed to be >0.9975 and the HCG ~ 0.9. The HCG period, bar width and thickness is designed to be 1150 nm, 700 nm and 450 nm respectively. The incident light polarization is TE, i.e. electrical field along the HCG bars. The static cavity length is 700 nm; with the reflection phase response of the designed HCG, this corresponds to the cavity resonance wavelength of ~ 1550 nm. Each HCG mirror is 20 µm by 20 µm in size, and 8x8 individual pixels form the whole optical phased array, with the pitch ~33.5 µm. The pixels are isolated from each other by deep trenches, and they are individually electrically addressable through the metal fanned-out lines. Figure 15 shows the SEM image of the fabricated device.
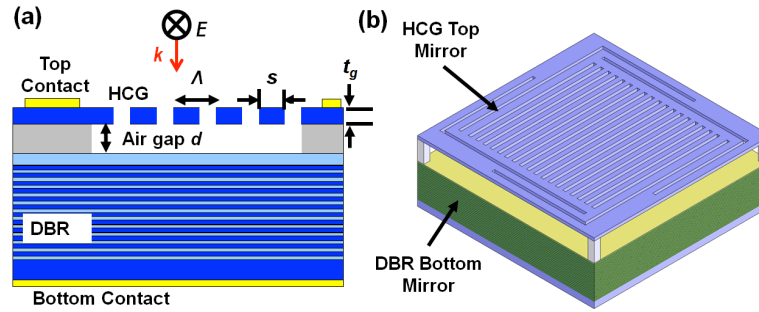

Figure 14. Schematic of an individual pixel of the optical phased array. The $Al_{0.6}Ga_{0.4}As$ HCG and 22 pairs of $GaAs/Al_{0.9}Ga_{0.1}As$ DBR serve as the top and bottom reflector of the Fabry-Perot etalon. The incident light is surface normal to the etalon, and polarized in parallel to the grating bar. Λ, HCG period; s, grating bar width; t_g, HCG thickness; d, air gap between HCG and DBR. We design Λ=1150 nm, s=700 nm, t_g=450 nm, and d=700 nm.
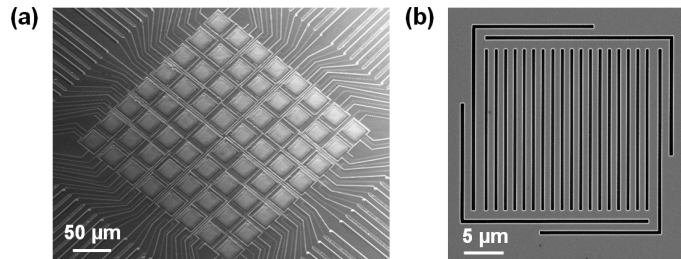

Figure 15. (a) SEM image of an 8x8 optical phased array. Each pixel is an HCG-APF, which can be individually electrically addressed by the fanned-out metal contacts. The pitch of the HCG mirror is

~33.5 μm. (b) Zoom-in view of the HCG mirror in a single pixel. The HCG mirror size (without the MEMS) is 20 μm by 20 μm.

The HCG can be actuated by applying a reverse electrical bias on the p-n junction between the HCG and DBR. This changes the cavity length and thus the reflection phase of the incident light. Figure 16(a) shows the reflection spectrum of a single HCG APF of the array, for different reversed bias. As the reversed bias increases, the cavity length decreases, resulting in a blue-shift of the resonance wavelength. The measured reflection spectrum is fitted with the standard FP etalon reflection formulation, and the top mirror and bottom mirror's reflectivity is extracted. The reflectivity of the bottom DBR is extracted to be 0.9965±0.0012, and the reflectivity of the top HCG increases from 0.955 to 0.976 as the wavelength decreases. The HCG reflectivity is higher than the designed value due to an inadvertent inaccuracy in electron beam lithography and etching process. The reflection phase of an individual etalon versus applied voltages is then characterized by a Michelson interferometer. The result is shown in Figure 16(b). A total phase change of ~1.7 π is achieved within 10 V actuation voltage range at a wavelength of 1550 nm. The actual displacement of the HCG can be extracted from Figure 16(a) and the cavity design. For this 1.7 π phase change, the HCG displacement is 50 nm. This demonstrates the high phase tuning efficiency of the APF. The reflectivity of the DBR and HCG can be extracted from this phase measurement by a curve fitting. They are extracted to be 0.9977 and 0.935 respectively, in a reasonably good match with the value extracted from the reflection spectrum measurement.
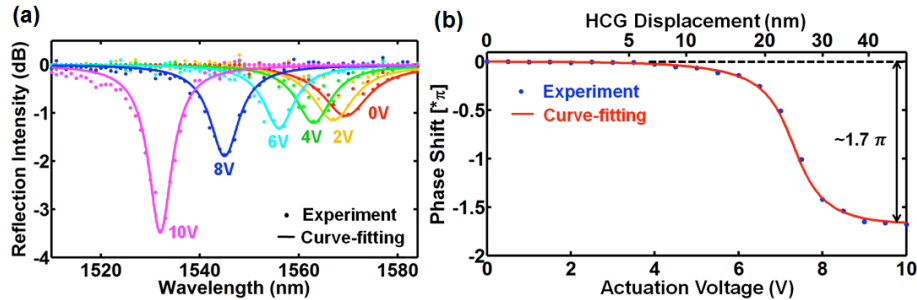

Figure 16 (a) Reflection spectrum of an HCG-APF with different actuation voltages. As the reversed bias voltage increases, the cavity length decreases, resulting in a blue-shift of the resonance wavelength. (b) Reflection phase shift versus applied voltage on a single HCG-APF of the phased array. ~1.7 π phase shift is achieved within 10 V actuation voltage range at a wavelength of 1550 nm; this corresponds to a displacement of ~50 nm of the HCG. The measured results are curve fitted to extract the reflectivity of the DBR and HCG.

The MEMS HCG is designed to have a high mechanical resonance frequency to facilitate a fast phase tuning. Two different methods are used to characterize the mechanical resonance frequency. The first one is LDV. A white-noise electrical signal is used to actuate the HCG. A laser is incident onto the HCG, and the Doppler shift of the reflection beam is recorded with respect to time, followed by a Fourier transform to reveal the information in the frequency domain, shown in Figure 17(a). The mechanical resonance frequency f_r is 0.53 MHz. Alternatively, a step voltage is applied to actuate the HCG mirror, and time resolved phase measurement can be

used to extract the mechanical resonance frequency. This time resolved phase trace is shown in Figure 17(b). The applied voltage changes from 6 V to 7 V at t=13.7 μs and back to 6 V at t=33.8 μs. A damped second harmonic oscillator model is used to analyze the ringing trace. The damped mechanical resonance frequency is extracted to be 0.52 MHz, in good agreement with the LDV measurement.
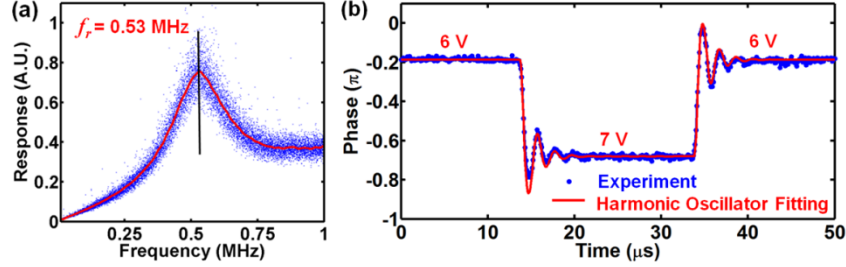

Figure 17. (a) Laser Doppler velocimetry measurement to characterize the mechanical resonance frequency of the HCG MEMS mirror. (b) Time resolved phase measurement of the HCG APF with a step voltage actuation signal. The blue dots are recorded in the experiment, and red traces are the simulated fitting curve from the second harmonic oscillator model.

To reduce the ringing, one can break the single voltage step into two steps, i.e. using input shaping technique. Instead of changing directly from 6 V to 7 V in the above example, we first change the voltage from 6 V to 6.5 V, hold it for 1 μs, and then change from 6.5 V to 7 V. The same applies for the case when the voltage changes from 7 V to 6 V. The 1 μs corresponds to about half of the ringing period, and thus the individual ringing from these two separate steps would have destructive interference, leading to an overall reduced ringing. The comparison between the single step and two-step voltage control is shown in Figure 18. The phase settles down much quicker when the two-step voltage control is used.
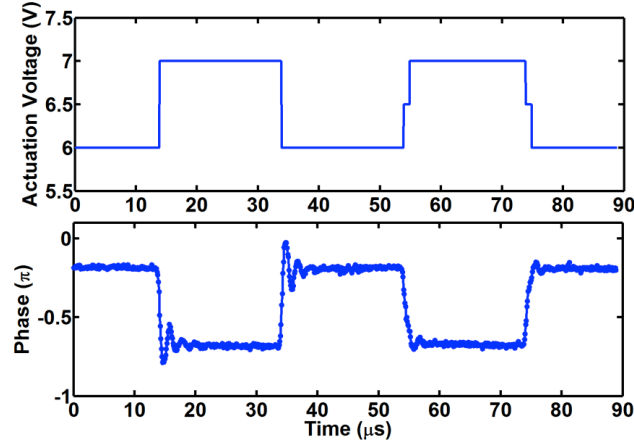

Figure 18. Comparison of the ringing between a single-step and two-step voltage control. In the two-step voltage control case, the time interval between the two different steps is 1 μs, corresponding to half of the ringing period. The individual ringing from these two separate steps would have destructive interference, leading to an overall reduced ringing.

Beam steering in far-field is achieved by creating the desired near-field phase front of the reflection beam on the whole 8x8 phased array. By controlling the applied voltage on each individual pixel of the HCG-APF array, the near-field phase pattern can be generated. The maximum steering angle is achieved when the phase is alternative between the pixels. This is also defined as half the total field of view (TFOV). Since the pitch of the pixel of the 8x8 array is 33.5 μm, the TFOV is 2.65°, for the operation wavelength of 1550 nm. To increase this, a two-lens system is used to magnify the beam steering angle. This angular magnification ratio is set to be 3.45 in the current experiment, and thus the TFOV is 9.14°.

Figures 6(a) and 6(c) shows various near-field phase patterns on the phased array, and the corresponding measured far field pattern. Both symmetric (column 2~5) and asymmetric (column 6~7) beam steering are performed. The TFOV is shown as the box in dashed line in Fig. 6(c). The strong zeroth order beam is due to the relatively low filling factor of the phased array (~36%). Quite a large portion of light gets reflected from the background with a fixed phase shift, contributing strongly to the zeroth order beam. The ratio between the total power of the steered beams and that of the zeroth order beam is measured to be ~0.5 in the best case. With the consideration of the filling factor, Fourier optics is applied to calculate the far-field patterns, shown in Fig. 6(b). The measured value of the full width beam divergence at the half power point (FWHM) is ~1°. This FWHM is determined by the total size of the array, calculated to be 0.33°, and magnified to be 1.14° by the lens. The experiment is in reasonably good agreement with the calculation results.
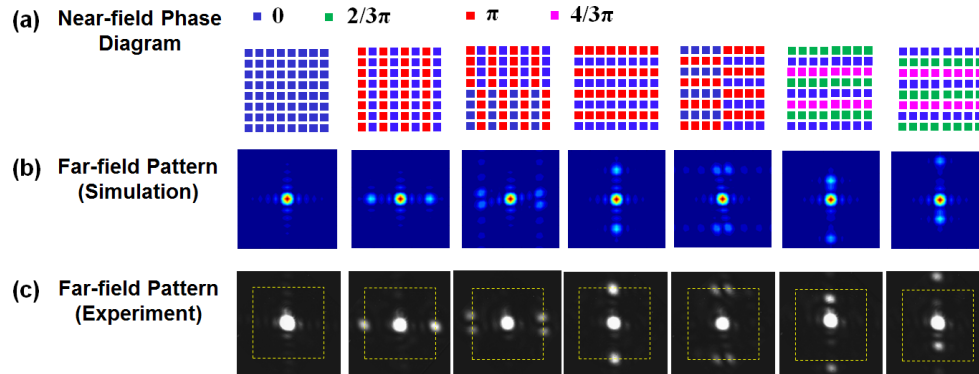

Figure 19. Beam steering experiment. (a) Near-field phase pattern created by the HCG-APF optical phased array. (b) The corresponding far-field pattern calculated by Fourier optics. (c) Experimentally measured far-field pattern, in reasonably good agreement with the calculation. The strong zeroth order beam is due to the relatively low filling factor of the phased array (~36%). The light that does not hit on the HCG-APF gets reflected with a fixed phase shift, contributing strongly to the zeroth order beam. The field of view of the image windows is 13° x 13°. The box in dashed line in (c) indicates the TFOV of the phased array (9.14° x 9.14°).

While we demonstrate its high-speed and low-voltage operation, there is much room to improve the overall performance of the all-pass filter array. Here we discuss the strategies. First of all, while the all-pass filter serves as a phase shifter for the incident beam, it also changes the power of the reflection beam. This is not desirable. To improve this, one can increase the reflectivity of the bottom DBR, by

increasing the number of pairs; and meanwhile slightly decrease the reflectivity of the top HCG. Both approaches reduce the reflection loss at the resonance. Secondly, due to the large number of pixel, there can appear some non-uniformity among the array pixels -- more specifically, the non-uniformity in the phase tuning curve. In the beam steering experiment, the deviation of the phase from its desired value in each pixel effectively scatters the light into the background and thus reduces the beam steering efficiency. To overcome this problem, one can actively monitor the phase and apply a feedback loop for the phase control on each individual pixel. Thirdly, both the TFOV and the divergence angle of the reflective beam from the phased array are important figure of merits. Their ratio determines the total number of resolvable spots across the TFOV in one dimension. This number is 8 in the device discussed above. The TFOV can be increased by reducing the pixel size; and the beam divergence angle can be decreased by scaling up the pixel numbers. Together, this will boost up the number of resolvable spots in TFOV. Fourthly, the zero-th order beam appears to be quite strong. To suppress it, one can increase the filling factor of the phased array. To demonstrate this, we design a high-filling factor array by grouping four pixels together without isolation trenches in between. Furthermore, two-dimensional HCG is designed and fabricated. The symmetric HCG can overcome the polarization sensitivity of the one-dimensional HCG. The two-dimensional HCG grid can also be actuated more uniformly. Figure 20(a) shows the SEM image of the two-dimensional HCG mirror for the HCG-AFP array. The HCG mirror size is 20 μm by 20 μm, and the filling factor is ~47%. Beam steering is experimentally demonstrated with the two-dimensional HCG-AFP, shown in Figure 20(b). Compared to the previous device, more power is being beam steered in this case. The ratio between the total power of the steered beams and that of the zero-th order beam is ~1.2. The increased power in the steered beam is also attributed to the improved pixel uniformity of the array. To further optimize the beam steering performance, a micro-lens array can be placed in front of the phased array, which can focus the input beam onto the HCG mirror of each pixel. This effectively increases the fill factor to 100%, and will ultimately suppress the zero-th order beam.
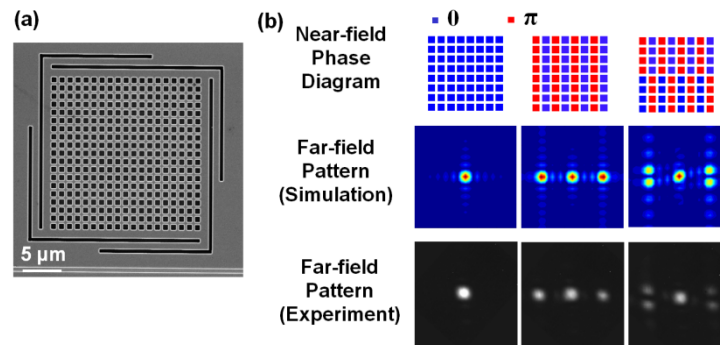
Figure 20. (a) SEM image of the two-dimensional HCG mirror for HCG-AFP array. (b) Beam steering experiment of the optical phased array using two-dimensional HCG as the top mirrors of the APF. Top panel, near-field phase pattern created by the HCG-APF optical phased array. Middle panel, the corresponding far-field pattern calculated by Fourier optics. Bottom panel, experimentally measured far-field pattern, in good agreement with the calculation.

The key advantage of using HCG APF is its high efficient phase tuning, i.e. small HCG MEMS mirror displacement (~50 nm) for large phase change (~1.7 π), and small voltage actuation (10 V) for fast beam steering (>0.5 MHz). The property of the HCG APF is also temperature independence, since the main cavity is made up of air. Both one-dimensional HCG and two-dimensional HCG are demonstrated as the top mirror for the APF. Beam steering is achieved by creating the desired near-field phase pattern on the HCG-APF array. Beam steering performance can be optimized by increasing the reflectivity of the bottom DBR, scaling up the pixel number while reducing the individual pixel size, as well as increasing the filling factor. We believe that by integrating a microlens array in front of the phased array, the effective fill factor can increase to 100%, leading to a greatly improved beam steering efficiency.

5.   Close-Loop Interferometic Control

In this section, we describe a high-speed optical beamsteering system based on an 8x8 MEMS phased array. The system incorporates an in-situ interferometer that provides a real-time, dynamic measure of the phase of each mirror in the array during beamsteering. A closed-loop phase-control algorithm results in <π/100 mirror phase accuracy and far field beam steering is shown. Stroboscopic measurement capabilities are demonstrated which allow us to show feedforward control to eliminate micromirror ringing.

The accuracy of beamsteering direction is a result of how accurate the phased array can reproduce the corresponding grating period. Both a finer phased array pitch and larger number or array elements result in more accurate beamsteering. The phase accuracy of individual array elements dictates the diffraction efficiency into the steered beam. For example, in the case of an 8x8 array, calculations reveal 3 dB diffraction efficiency loss in the steered beam results from ±0.4π random phase error.

In our work, we have created an 8x8 array of HCG mirrors that use electrostatic actuation to create a variable phase delay. The 8x8 version of this array was selected for this study since the individual voltage control of 64 mirrors is manageable while the total area of the array (280 x 280 μm) is large enough to limit the beam divergence to 5.5 mrad at c-band wavelengths. We design these mirrors to reflect 1550 nm light with 99% reflectivity and 20 V drive signal to produce at least 775 nm stroke (2π reflected phase shift). However, the ideal actuation response is rarely realized as reality introduces errors from fabrication and environmental influences during operation. These phase errors manifest themselves as a loss of diffraction efficiency and pointing accuracy. While these can and will be improved by refining the fabrication process, our goal here is to show that these problems are also corrected through our closed loop feedback operation. This paper describes a high-speed optical beamsteering system based on the 8x8 MEMS phased array. The system incorporates an in-situ interferometer that provides a real-time, dynamic measure of the phase of each mirror in the array

during beamsteering. This holds advantages over capacitive sensing which is subject to parasitic capacitance from external instruments and requires large structures (e.g. comb drives) to achieve nanometer resolution. To compensate for slow, time-varying phase errors resulting from thermal and electromechanical drift in the optical system, a closed-loop phase-control algorithm ensures accuracy of the phase settings to achieve a desired far-field beam pattern.

The optical component of our system has three functions: 1) measure individual mirror reflected phase delays, 2) create a collimated beam on the phased array and 3) deliver a steered beam. Commercial microscopic interferometric imaging systems view the sample under a microscope objective which makes the latter two requirements difficult to realize, so we designed the optical assembly shown in Figure 21. We use a fiber-collimating lens (Thorlabs PAF-X-5-C) and an additional focusing lens (AC254-150-C-ML, f = 15 cm) to create a collimated 332 µm diameter Gaussian beam that fits the MEMS device. This collimation requires two lenses to situate the device within the limited Rayleigh range.

The phase measurements are obtained through phase shifting interferometry (PSI). Our interferometer is composed of a series of a polarization beamsplitters and half wave plates to adjust the powers in the reference, measurement and output beams. Since we want to illuminate the device at normal incidence, we use a Faraday rotator to circulate the collinear reflected light through the adjacent polarization beamsplitter. The array is rotated 45° to match the incident polarization. A computer controlled Thorlabs Nanomax-600 stage supports and translates the MEMS device to produce adequate phase shifts for PSI. For microscopic imaging, we perform $4f$ image relaying with a pair of matched 10 cm focal length lenses to achieve 7.5 µm imaging resolution; sufficient to distinguish individual mirrors in the MEMS array. This image relaying system is necessary to keep the magnification microscope objective away from the sample and allow for steered output. The relayed image is magnified by a 10X microscope objective which forms the image on an InGaAs sensor array infrared (IR) camera (Xenics Bobcat-1.7-320) which is required to view 1550 nm wavelengths. The phase of each camera pixel is determined by translating the MEMS device using the stage and observing the resulting sinusoidal variation in intensity (PSI). We used 10 steps in triangular fashion (5 forward and 5 back), covering one full period, and extracted the phase using a least squares fit. The frame rate of the camera and the speed of the translation stage enable a measurement of the displacement of all the MEMS mirrors about once every second. Since we are interested in only the mirror movements, any phase aberrations are removed by subtracting a reference phase map of the MEMS mirrors at rest. The camera is capable of stroboscopically measuring MHz MEMS movements with 80 ns frame integration times. Since we gate the image instead of the illumination source, the laser can be continuous and the system can maintain high power for beam steering.

The steered beam output of our device is separated at the top right corner in Figure 21. At this point, the reflected device output is Fourier transformed by one of

the image relaying lenses. To restore the steered beam, we use another confocal lens. By selecting a smaller focal length lens here, we can arbitrarily increase the total beamsteering field of view.
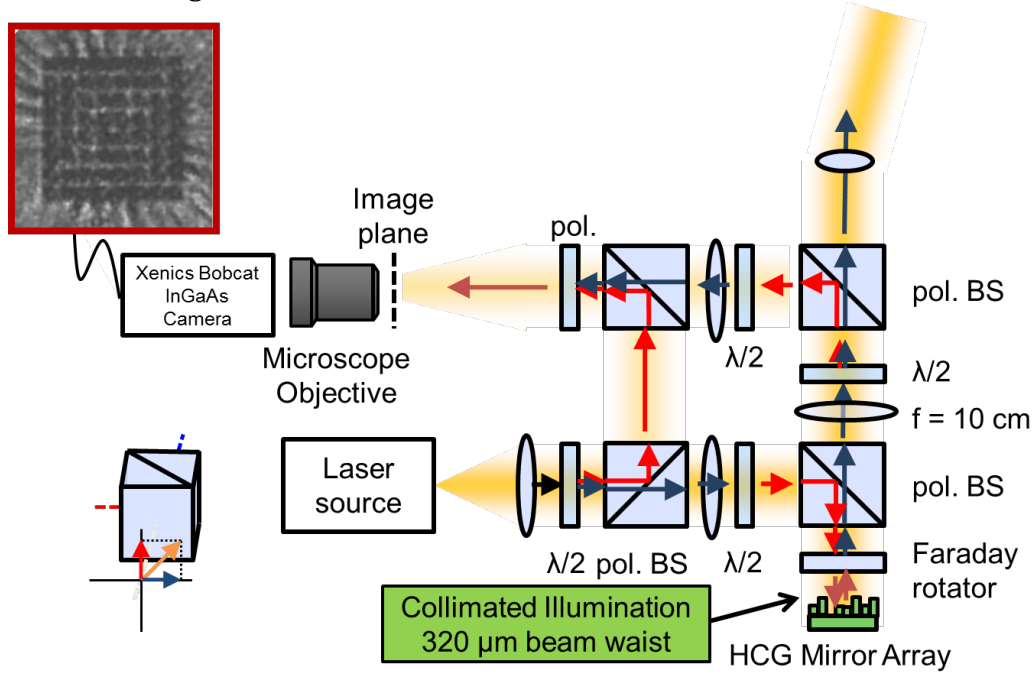

Figure 21. Diagram of the optical system. A series of polarization beamsplitters and half wave plates form the two arms of an interferometer. Two lenses create a collimated illumination spot that fits the MEMS device. The measurement arm of the interferometer includes a 4*f* imaging system to preserve the imaging resolution and keep the imaging optics from blocking the steered device output. The output is extracted at the top right of the diagram, and magnified with a confocal lens with smaller focal length.

We can optionally remove the Faraday rotator to suppress background light reflecting from the wafer substrate. The mechanism behind this is as follows. Light reflecting from the background substrate maintains its polarization state that corresponds to the reflection mode of the polarization beamsplitter. The light from the HCG mirrors interacts with 45° rotated HCG mirror whose polarization dependence separates the light into two orthogonally polarized components. These are the HCG's TE and TM modes that now introduce power in the polarization beamsplitter's transmission path. There is an associated 3 dB loss from 45° polarized light passing through the polarization beamsplitter cube, but this tradeoff is acceptable when the device fill factor is small or when the array is overfilled by the illuminating beam spot.

Using our ability to measure the phase of each HCG mirror, we can adjust the control voltages to achieve the desired phase levels through closed loop control, as illustrated in Figure 22. Here, the initial control voltage is generated from a look-up table. The closed loop control subsequently adjusts the voltage until the desired phase is observed. The speed of one iterative loop is limited by the long (~0.1 second) response time of the phase shifter required for PSI. Nevertheless, this

speed is sufficient for initially setting and periodically updating the look-up table for initial device calibration and correction for long term drift.
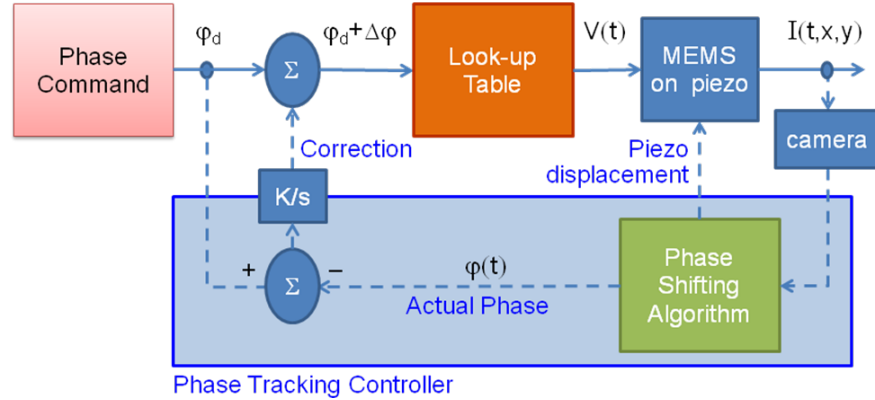

Figure 22. Closed loop feedback control diagram. Control voltages are defined for phase setpoints with feedback control to compensate for long term drift.

Our micromirrors are supported by elastic structures which exhibit damped harmonic oscillations that extend the mirror's settling time. Feedforward drive signal shaping can mitigate these oscillations and effectively minimize the slew rate for rapid beam steering. Our Xenics Bobcat-1.7-320 imager can have short (<1 μs) integration windows to measure the mirror dynamic response stroboscopically. To measure the mirror dynamic response, we actuated a single mirror with a periodic square pulse that was synchronized to the 1 μs camera integration window. The square wave followed the camera trigger by a variable delay that was scanned to create a transient measurement. Our phase shift calculations from these images produce the transient response shown in the first plot in Figure 23. This shows damped oscillation with a 1.82 μs damping time constant and 232 kHz resonance when the mirror is pulled down. The oscillation lasts only a few cycles, due to squeeze film damping of the mirror that is operating in air at atmospheric pressure. Even so, the sudden step results in a sizeable overshoot. To eliminate the oscillations, we applied a feedforward control signal consisting of two voltage steps. The elimination of ringing is accomplished by using an intermediate voltage step which makes the phase peak at our desired phase setpoint, then stepping the voltage again, right at the moment when the displacement is largest, setting the voltage to the final level which holds the mirror steady. The second half of Figure 23 shows the corresponding transient response where the settling time is now reduced by more than an order of magnitude.
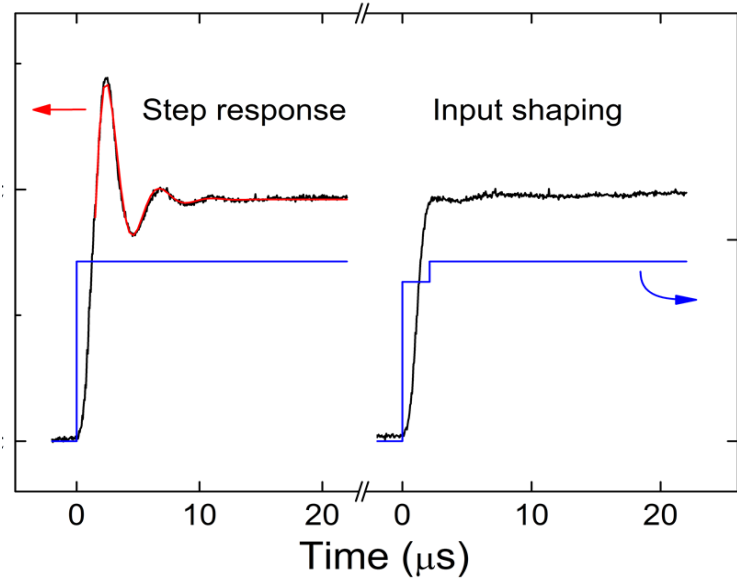
Figure 23. Transient response of a mirror actuated with a voltage step and with a shaped signal to eliminate harmonic oscillations.

Figure 24 reveals the feedback control ability of our system on a single mirror phase. In these measurements, we target a 1.0 π phase setpoint and adjust the device temperature using a thermoelectric cooler in contact with the device. Section I of the figure shows the voltage level being adjusted to maintain the phase level with approximately π/100 rms deviation. In section II, the voltage level is maintained to show how the mirror phase would drift under open-loop control. The drift is significant (0.2 π with 4°C temperature change) and further demonstrates the need for closed loop phase control. Section III shows closed-loop feedback used to restore the 1.0 π mirror phase. Note that the voltage level required to maintain 1.0 π phase at 21°C in section III has changed from section I despite the same device temperature. It is not yet clear why this occurs.
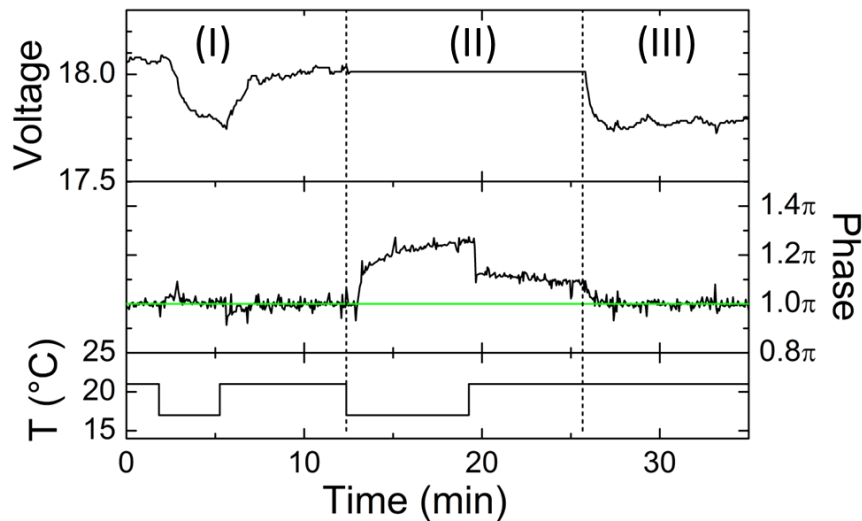
Figure 24. Demonstration of phase control of a single mirror with a 1.0 π phase shift target. The plot shows three periods with closed-loop phase control on, off and on, respectively. The temperature is switched between 21°C and 17°C to induce a mirror response drift in the first two periods.

We demonstrate the beamsteering ability of the phased array by imposing a diagonal phase gradient. This was set to steer the beam to half of the maximum achievable beamsteering angle defined by the Nyquist criterion. The desired and measured phase patterns are shown in Figure 25. Due to mirror nonuniformity and crosstalk in these first generation devices, we are only able to achieve accurate phase patterns using the closed loop feedback system. Obviously, the dead mirrors remain stationary and appear with 0 phase shift in the measured phase pattern. Using the far field Fourier diffraction theorem [9], we show the expected far field pattern from a flat array in Figure 26(a), the far field pattern when the phase gradient is applied in Figure 26(b), and the comparison of the two in a line plot in Figure 26(c). Figure 26(d)-(f) are the experimentally measured results corresponding to these calculations, captured by the camera. Since the observed angles are dictated by the magnification system, we normalized the angles according to the period of the phased array. We calculated the contribution of zeroth order light from the device substrate and subtracted it from the measurements to show contrast in the steered beam. The similarities between the far field pattern and the calculations verify the effectiveness of our closed loop feedback system.
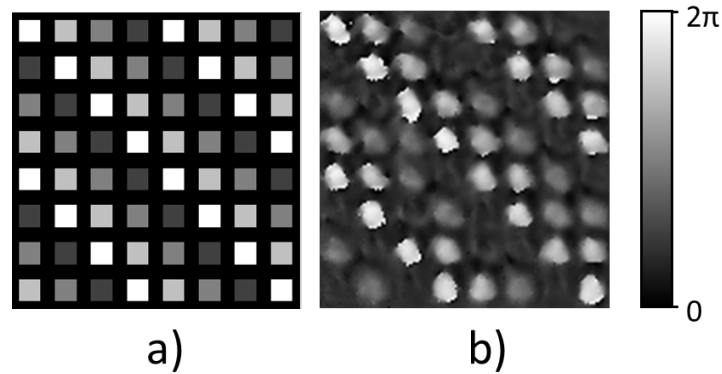

a)   b)

Figure 25. (a) Target and (b) measured phase patterns. The measured phase pattern was achieved using closed loop feedback.
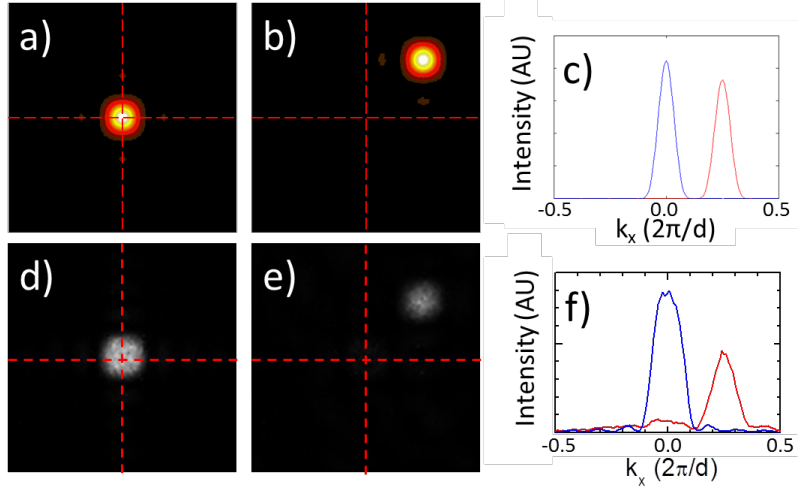
Figure 26. Calculated and measured far field patterns of reflected light from the phased array. Calculated reflection from (a) a flat array, (b) a diagonal phase gradient and (c) their cross section plotted together. Measured reflection from (d) a flat array, (e) a diagonal phase gradient and (f) their cross section plotted together.

Most of our optical power is lost since the mirrors only cover a small portion of the incident beam. As stated earlier, the HCG mirrors have 20 µm widths on a 35 µm mirror pitch. A 332 µm diameter Gaussian spot illuminates the array, overfilling it for an inherent 7.03 dB insertion loss. Since the fill factor is small, we choose to use the system without a Faraday rotator to eliminate the background light. We measure 7.12 dB insertion loss after correcting for the 50% power throughput caused by the absence of a Faraday rotator. We can decrease the insertion loss in two ways: by increasing the mirror fill factor and by decreasing the spot size relative to the array. Increasing the fill factor will also increase diffraction efficiency by decreasing the power in the side lobes. To decrease the relative spot size, the beam spot size can be reduced or the array size can be expanded with either larger mirrors or more array elements. Expansion of the mirrors leads to the expansion of the array period, and the spatial frequency of the array decreases along with the total beamsteering range. This also creates heavier MEMS HCG mirrors which slow down the operation speed. The preferable alternative is to add more mirrors to the array which also creates a less divergent beam; the tradeoff for this is additional complexity in the fabrication and control of more mirrors. This modification will be presented in future publications.

Similar to the stroboscopic measurements of individual mirror phase response, we took stroboscopic measurements of the far field by projecting it onto the camera sensor and synchronizing the drive voltage to the camera frame rate. A binary phase checkerboard pattern was used with a single voltage level to create 4 first order diffraction spots in the far field. We integrated the intensity of the diffracted and central beams to plot their transient response. As with single mirror displacement, this also exhibited damped harmonic oscillations. In this case, an overshoot in the mirror displacements leads to a loss of diffraction efficiency and decrease in measured diffracted power. This ceiling effect produces an oscillating

intensity with twice the resonance frequency. With this accounted for, we measured 182 kHz resonances with a 2.2 µs damping coefficient with pull down. These measurements are 317 kHz resonances with 2.8 µs damping coefficient with release. This is three times faster than previously reported MEMS pistons mirror arrays.

In this program, we developed a beamsteering system which provides closed-loop feedback control of a two-dimensional optical phased array of high contrast grating mirrors. Closed loop feedback is accomplished simultaneously with device output, using only a small percentage of the optical power. Individual mirror calibration becomes unnecessary as closed loop feedback only requires the definition of phase setpoints. This feedback also allows for in-situ correction of phase drift that occurs with device use and environmental changes. With this system, we demonstrated <π/100 phase control accuracy and performed beamsteering with better than 2.5% pointing accuracy. Stroboscopic measurements by gated imaging reveal the dynamic response of the mirror motion and far field response, showing damped harmonic motion with 320 kHz resonance. The ability to measure the dynamic response allows us to show the elimination of the harmonic motion using feedforward waveform shaping.

6. Publications

[1]–[11]

[1]   B.-W. Yoo, M. Megens, T. Sun, W. Yang, C. J. Chang-Hasnain, D. A. Horsley, and M. C. Wu, "A 32 × 32 optical phased array using polysilicon sub-wavelength high-contrast-grating mirrors," *Optics Express*, vol. 22, no. 16, p. 19029, Aug. 2014.
[2]   W. Yang, T. Sun, Y. Rao, M. Megens, T. Chan, B.-W. Yoo, D. A. Horsley, M. C. Wu, and C. J. Chang-Hasnain, "High speed optical phased array using high contrast grating all-pass filters," *Optics Express*, vol. 22, no. 17, p. 20038, Aug. 2014.
[3]   B.-W. Yoo, M. Megens, T. Chan, T. Sun, W. Yang, C. J. Chang-Hasnain, D. A. Horsley, and M. C. Wu, "Optical phased array using high contrast gratings for two dimensional beamforming and beamsteering," *Opt. Express*, vol. 21, no. 10, pp. 12238–12248, May 2013.
[4]   T. K. Chan, M. Megens, B.-W. Yoo, J. Wyras, C. J. Chang-Hasnain, M. C. Wu, and D. A. Horsley, "Optical beamsteering using an 8x8 MEMS phased array with closed-loop interferometric phase control," *Optics Express*, vol. 21, no. 3, p. 2807, Jan. 2013.
[5]   M. Megens, B.-W. Yoo, T. Chan, W. Yang, T. Sun, C. J. Chang-Hasnain, M. C. Wu, and D. A. Horsley, "High-speed 32×32 MEMS optical phased array," 2014, vol. 8977, p. 89770H–89770H–7.
[6]   M. Megens, B.-W. Yoo, T. Chan, W. Yang, T. Sun, C. J. Chang-Hasnain, M. C. Wu, and D. A. Horsley, "High-contrast grating MEMS optical phase-shifters for two-dimensional free-space beam steering," 2014, vol. 8995, p. 89950Q–89950Q–8.
[7]   B.-W. Yoo, T. Chan, M. Megens, T. Sun, W. Yang, Y. Rao, D. A. Horsley, C. J. Chang-Hasnain, and M. C. Wu, "Optical phased array using single crystalline silicon high-contrast-gratings for beamsteering," in *Proc. SPIE 8633, High Contrast Metastructures II, 86330F*, 2013, vol. 8633, p. 86330F–86330F–6.

[8] B. W. Yoo, M. Megens, T. K. Chan, T. Sun, W. Yang, D. . Horsley, C. J. Chang-Hasnain, and M. C. Wu, "32x32 Optical phased array with ultra-lightweight high-contrast-grating mirrors," in *2013 Transducers Eurosensors XXVII: The 17th International Conference on Solid-State Sensors, Actuators and Microsystems (TRANSDUCERS EUROSENSORS XXVII)*, 2013, pp. 2505–2508.

[9] W. Yang, T. Sun, Y. Rao, T. Chan, M. Megens, B.-W. Yoo, D. A. Horsley, M. C. Wu, and C. J. Chang-Hasnain, "Optical phased array using high-contrast grating all-pass filters for fast beam steering," in *Proc. SPIE 8633, High Contrast Metastructures II, 86330F*, 2013, vol. 8633, p. 86330G–86330G–5.

[10] B.-W. Yoo, T. Chan, M. Megens, T. Sun, W. Yang, F. Rao, C. Chang-Hasnain, D. A. Horsley, and M. C. Wu, "Fast optical phased array with ultra-lightweight high-contrast-grating mirrors," in *2012 International Conference on Optical MEMS and Nanophotonics (OMN)*, 2012, pp. 144–145.

[11] W. Yang, T. Sun, Y. Rao, M. Megens, T. Chan, B.-W. Yoo, D. A. Horsley, M. C. Wu, and C. J. Chang-Hasnain, "High-speed optical phased array using high-contrast grating all-pass filters," in *2012 International Conference on Indium Phosphide and Related Materials (IPRM)*, 2012, pp. 22–24.